Center for Environmentally Sustainable Transportation in Cold Climates
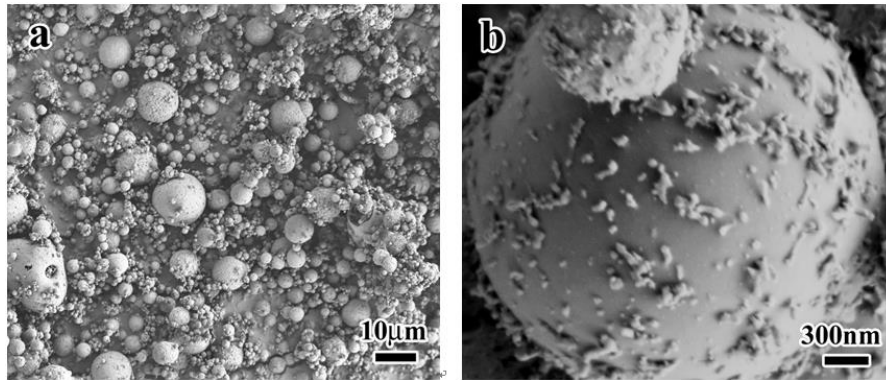
Development of durable "green" concrete exposed to deicing chemicals via synergistic use of locally available recycled materials and multi-scale modifiers

Prepared by:

Ning Xie, Ph.D.
Western Transportation Institute, Montana State University

Na Cui, Ph.D.
Western Transportation Institute, Montana State University

February 2018

REPORT DOCUMENTATION PAGE

Form approved OMB No.

1. AGENCY USE ONLY (LEAVE BLANK)	2. REPORT DATE 2/2018	3. REPORT TYPE AND DATES COVERED Final Report: 06.15.2015 – 07.15. 2017

4. TITLE AND SUBTITLE

Development of durable "green" concrete exposed to deicing chemicals via synergistic use of locally available recycled materials and multi-scale modifiers

5. FUNDING NUMBERS
INE/CESTiCC 1502

6. AUTHOR(S)
Name, Title, Organization/University
Ning Xie, and Na Cui

7. PERFORMING ORGANIZATION NAME(S) AND ADDRESS(ES)

Center for Environmentally Sustainable Transportation in Cold Climates
University of Alaska Fairbanks
Duckering Building Room 245
P.O. Box 755900
Fairbanks, AK 99775-5900

8. PERFORMING ORGANIZATION REPORT NUMBER

INE/CESTiCC 1502

9. SPONSORING/MONITORING AGENCY NAME(S) AND ADDRESS(ES)

U.S. Department of Transportation
1200 New Jersey Avenue, SE
Washington, DC 20590

10. SPONSORING/MONITORING AGENCY REPORT NUMBER

11. SUPPLENMENTARY NOTES

12a. DISTRIBUTION / AVAILABILITY STATEMENT

No restrictions

12b. DISTRIBUTION CODE

13. ABSTRACT (Maximum 200 words)

From the economic and social perspectives, the use of waste materials would not be attractive until their costs and quality can satisfy the construction requirements. In this study, a pure fly ash paste (PFAP) was developed in place of ordinary Portland cement paste (OPCP). This PFAP was prepared at room temperature and without direct alkali activation. The samples were prepared using only the as-received class C coal fly ash, water, and a very small amount of borax ($Na_2B_4O_7$). On average, the PFAP featured 28-d compressive strength of about 36 MPa, and micro-nano hardness and elastic modulus 29% and 5%, higher than the OPCP, respectively. These mechanical and other properties of the PFAP make it a viable "green" construction binder suitable for a host of structural and non-structural applications. Advanced characterization of the raw material and PFAP pastes was employed to elucidate the hydration mechanisms of this "green" binder. The obtained knowledge sheds light on the role of class C CFA in the hydration process and may benefit the expanded use of various CFAs in cementitious materials.

14- KEYWORDS :
waste materials recycling; pure fly ash; cementitious binder; hydration process mechanisms

15. NUMBER OF PAGES
54

16. PRICE CODE
N/A

17. SECURITY CLASSIFICATION OF REPORT	18. SECURITY CLASSIFICATION OF THIS PAGE	19. SECURITY CLASSIFICATION OF ABSTRACT	20. LIMITATION OF ABSTRACT
Unclassified	Unclassified	Unclassified	N/A

DEVELOPMENT OF DURABLE "GREEN" CONCRETE EXPOSED TO DEICING CHEMICALS VIA SYNERGISTIC USE OF LOCALLY AVAILABLE RECYCLED MATERIALS AND MULTI-SCALE MODIFIERS

FINAL REPORT

Prepared for

Center for Environmentally Sustainable Transportation in Cold Climates

Authors:

Ning Xie, Ph.D.,
Montana State University
Western Transportation Institute

Na Cui, Ph.D.
Montana State University
Western Transportation Institute

INE/AUTC 17.04

January 2018

DISCLAIMER

METRIC (SI*) CONVERSION FACTORS

APPROXIMATE CONVERSIONS TO SI UNITS

Symbol	When You Know	Multiply By	To Find	Symbol
		LENGTH		
in	inches	25.4		mm
ft	feet	0.3048		m
yd	yards	0.914		m
mi	Miles (statute)	1.61		km
		AREA		
in^2	square inches	645.2	millimeters squared	cm^2
ft^2	square feet	0.0929	meters squared	m^2
yd^2	square yards	0.836	meters squared	m^2
mi^2	square miles	2.59	kilometers squared	km^2
ac	acres	0.4046	hectares	ha
		MASS (weight)		
oz	Ounces (avdp)	28.35	grams	g
lb	Pounds (avdp)	0.454	kilograms	kg
T	Short tons (2000 lb)	0.907	megagrams	mg
		VOLUME		
fl oz	fluid ounces (US)	29.57	milliliters	mL
gal	Gallons (liq)	3.785	liters	liters
ft^3	cubic feet	0.0283	meters cubed	m^3
yd^3	cubic yards	0.765	meters cubed	m^3

Note: Volumes greater than 1000 L shall be shown in m^3

Symbol	When You Know	Multiply By	To Find	Symbol
		TEMPERATURE (exact)		
ºF	Fahrenheit temperature	5/9 (ºF-32)	Celsius temperature	ºC
		ILLUMINATION		
fc	Foot-candles	10.76	lux	lx
fl	foot-lamberts	3.426	candela/m^2	cd/cm^2
		FORCE and PRESSURE or STRESS		
lbf	pound-force	4.45	newtons	N
psi	pound-force per square inch	6.89	kilopascals	kPa

These factors conform to the requirement of FHWA Order 5190.1A *SI is the symbol for the International System of Measurements

APPROXIMATE CONVERSIONS FROM SI UNITS

Symbol	When You Know	Multiply By	To Find	Symbol
		LENGTH		
mm	millimeters	0.039	inches	in
m	meters	3.28	feet	ft
m	meters	1.09	yards	yd
km	kilometers	0.621	Miles (statute)	mi
		AREA		
mm^2	millimeters squared	0.0016	square inches	in^2
m^2	meters squared	10.764	square feet	ft^2
km^2	kilometers squared	0.39	square miles	mi^2
ha	hectares (10,000 m^2)	2.471	acres	ac
		MASS (weight)		
g	grams	0.0353	Ounces (avdp)	oz
kg	kilograms	2.205	Pounds (avdp)	lb
mg	megagrams (1000 kg)	1.103	short tons	T
		VOLUME		
mL	milliliters	0.034	fluid ounces (US)	fl oz
liters	liters	0.264	Gallons (liq)	gal
m^3	meters cubed	35.315	cubic feet	ft^3
m^3	meters cubed	1.308	cubic yards	yd^3

Symbol	When You Know	Multiply By	To Find	Symbol
		TEMPERATURE (exact)		
ºC	Celsius temperature	9/5 ºC+32	Fahrenheit temperature	ºF
		ILLUMINATION		
lx	lux	0.0929	foot-candles	fc
cd/cm^2	candela/m^2	0.2919	foot-lamberts	fl
		FORCE and PRESSURE or STRESS		
N	newtons	0.225	pound-force	lbf
kPa	kilopascals	0.145	pound-force per square inch	psi

```
           32        98.6            212ºF
-40ºF   0     40     80    120   160   200

-40ºC  -20          20    40   60   80
              0          37          100ºC
```

ACKNOWLEDGMENTS

TABLE OF CONTENTS

LIST OF FIGURES

LIST OF TABLES

EXECUTIVE SUMMARY

This study focused on preparing a novel pure fly ash paste (PFAP) as a potential replacement for the cement paste, in order to reduce the life cycle environmental footprint of cementitious materials. The PFAP was successfully prepared at room temperature with an as-received coal fly ash, borax, and with water/binder ratio of 0.2.

The hardened pure fly ash paste exhibited a reasonable 28-d compressive strength (36 MPa), rapid strength gain (19MPa and 31 MPa in 1d and 3d, respectively), low bulk dry density (1.6 g/cm^3), very high electrical resistivity, outstanding micro-nano hardness and elastic modulus, low gas permeability coefficient (4.1×10^{-17} m^2/s), reasonably low Cl$^-$ diffusion coefficient (1.9×10^{-12} m^2/s), a denser microstructure, and better heat resistance than the ordinary Portland cement paste. The properties of the PFAP make it a viable "green" construction binder suitable for a host of structural and non-structural applications.

The hydration mechanisms of this "green" binder were presented by characterizing the raw material and PFAP pastes via XRF, SEM/EDS, XRD, and DSC/TGA approaches. The data reveal that the hydration of the PFAP is very complex and likely entails reactions between the free Ca^{2+}, Fe^{3+}, Al^{3+}, and Mg^{2+} and silicates to form amorphous Al-rich and Fe-rich binder phases.

While this work only showcases the properties of one specific PFAP, the obtained knowledge sheds light on the role of class C PFAP in the hydration process and may benefit the expanded use of various PFAP s in the manufacturing of paste, mortar, and concrete materials.

CHAPTER 1. INTRODUCTION

1.1 Problem Statement

Construction activities can have many negative environmental impacts. The hierarchy of disposal options to the environmental impacts can be categorized into six levels from low to high, namely, reduce, reuse, recycle, compost, incinerate and landfill. Before a recyclable material can be utilized in a field, the economy, compatibility with other materials, and material properties should be considered as the main three concerns. From the economic perspective, the use of waste materials would not be attractive until their costs and quality can satisfy the construction requirements.

The production of Portland cement (the most common binder in concrete) is an energy-intensive process that accounts for a significant portion of global CO_2 emissions and other greenhouse gases. In addition, as another energy intensive industry, pavement construction and maintenance activities also pose tremendous negative environmental impacts, such as greenhouse gases emissions and landfilling problems of waste materials. With increasing energy costs and heightened concerns about the environmental footprint of infrastructures' construction and maintenance activities, there has been a steady increase in interest and research activity on the use of other recycled materials in concrete infrastructure. Therefore, it is indispensable to develop new technologies, which can expand the application of recycled materials, to reduce the costs of concrete constructions and maintenance effort, and improve waste management and recycling process.

The re-use of low-cost or recycled materials for preparing "green" concrete has increasingly attracted attention of the concrete industry in recent years. Yet research is lacking in the synergistic use of multi-scale modifiers and low-cost or recycled materials for high performance cementitious binders. While the use of nano-/micro-sized materials and

recycled materials in cementitious concrete infrastructure has increased, along with a growing

body of positive evidence or user experience, a study to leverage the recent advances and

focus on the cold climate user requirements is needed and timely. The current knowledge

gaps have hindered development in this area and the effort to balance construction cost and

overall performances of cementitious concrete infrastructure.

1.2 Background

It has been widely accepted that the realization of sustainability should be focused on

three aspects, namely, economy, society and environment. To facilitate the sustainable

development of pavement and bridge engineering, not only direct economic costs and social

benefits from construction process should be considered, additional effort should be made to

quantify and minimize the indirect costs resulting from their environmental footprint.

The freeze/thaw damage and impacts from the use of deicing chemicals are important

factors that aid in determining the durability of the concrete pavement and bridge decks. A

reduction in performance and service live of the concrete infrastructure can lead to a

significant cost increases in preventative maintenance and rehabilitation activities. Although

some technologies may improve durability of the concrete infrastructure, some of these

technologies may also increase cost and may sacrifice some basic performances of the

cement concrete.

1.3 Objectives

The objective of this project is to develop a new technology by synergistically using

local low-cost or recycled materials to prepare "green" cementitious binder. In this project,

we are trying to find a balance between the performance and the environmental benefits

through the use of recycled materials as cementitious binders. This study will focus on the

formulation and property testing of the overall performance of the developed "green" binder,

with a focus on testing performance at low temperatures, including freeze/thaw and salt scaling resistance.

1.4 Research Methodology

In this project, the low-cost recycled material, namely the coal fly ash, has been employed to fabricate sustainable cementitious binders. Key properties of the binders, including freeze/thaw and salt scaling resistance has been tested. For the optimized binder formulations, the reaction mechanisms have been elucidated by microstructure and chemical analysis.

In this project, appropriate mix designs for pavements have been developed and the strength and durability of the "green" concrete has been tested based on related ASTM and AASHTO standards and specifications.

Task 1. Develop appropriate mix designs for samples

This task has identified and evaluated the low-cost recycled materials, namely the coal fly ash, as "green" cementitious binders. A mix design of the "green" concrete has been developed. Small amounts of surfactant were used to "neutralize" and block the free carbon in the high-LOI fly ashes (e.g., LOI between 5% to 8%). This approach is a promising way to ensure that the free carbon in the fly ash would not significantly undermine the properties of fresh or hardened concrete.

Once the mix designs of the control concrete were finalized, this task was entail fabrication of the "green" concrete to be further tested and examined in later tasks. The effect of water/binder ratio and curing regime (relative humidity, temperature, time) on the properties of both fresh and hardened concrete has been explored. Cost, properties, and "greenness" (amount of fly ash used) have been taken into account when defining the optimum.

Task 2. Determining modifier types of "green" binders

4

The realization of the "green" concrete will mostly build on the success of previous WTI research. Patents and other published literature have been examined to understand the state of the art and identify useful constituents for eco-friendly cementitious binders. The selected materials should pose minimal toxicity to the environment, originate from eco-friendly processes, and/or reduce the final product cost. Local low-cost recycled materials – coal fly ash was used as the cementitious binders. Initial screening of binder formulations were based on two key performance parameters of the nano-modified "green" binder, i.e., freeze/thaw and salt scaling resistance. The "green" cementitious binder has been tested at -25°C ~ +25°C for its freeze/thaw damage resistance property and two types of deicing chemicals was used for the salt scaling resistance evaluation.

A statistical design of experiments (DoE) has been employed to investigate the interactions between the influential factors and the performance parameters of a host of cementitious binder formulations. This task will involve testing compressive strength (ASTM C39-2014), splitting tensile strength (ASTM C496-2011), mass loss, and gas permeability of the cementitious binders to identify mixes appropriate for the "green" concrete preparation.

Task 3. Advanced characterization of the modified "green" binders

Advanced characterization tools, including Scanning electron microscopy (SEM), Differential Scanning Calorimetry/Thermogravimetric Analysis (DSC/TGA), has been applied to analyze the microstructures and phase change information of select "green" cementitious binders. The SEM/EDS analysis provided information on the elemental distribution along the fracture surfaces of the cementitious binders (without damage which can result from the high energy electron beam), and DSC/TGA provided details of phase change information to the specimen of interest. Nano- and micro-analysis using SEM/EDS provided the localized morphological and elementary information of the binders. The

findings from this task help to expand the applications of low-cost recycled materials, which can further improve the performances of the "green" cementitious binders.

Task 4. Final report and presentation

A final report has been prepared and submitted to CESTiCC. This task involves analyzing the experimental data, preparing a final report that documents the background information, methodology, and research findings associated with this project, and conducting the final presentation.

CHAPTER 2. LITERATURE REVIEW

The production of cement is an energy-intensive process that constitutes a significant portion of anthropogenic carbon dioxide emissions and other greenhouse gases (Van Dam et al. 2010; Lei et al. 2011; Hasanbeigi et al. 2012). Concrete is the most widely used man-made building material in the world, and its annual global production is approximately 5.3 billion cubic meters (Roskos et al. 2011). Cement is the most common binder in concrete, and its annual global production "has reached 2.8 billion tons (t), and is expected to increase to some 4 billion tons" (Schneider et al. 2011). Durability and sustainability are two increasingly important characteristics for concrete infrastructure (Shi et al. 2012; Kayali et al. 2013; Zhang et al. 2013), and numerous studies have been dedicated to the use of industrial wastes as supplementary cementitious materials (SCMs) in concrete without sacrificing its long-term performance and reliability (Khatri et al. 1995; Akkaya et al. 2007; Elahi et al. 2010; Johari et al. 2011; Shi et al. 2011; Lothenbach et al. 2011).

Coal fly ashes (CFAs) are the main by-products of coal combustion for electrical energy production. They are considered as a type of solid waste with high levels of contaminants, and thus pose a substantial environmental risk unless being solidified in concrete or mortar (Fytianos et al. 1998; Popovic et al. 2001). The U.S. generates approximately 70 million tons of CFAs, of which only 27 percent (~19 million tons) are recycled and the rest are landfilled (Rostami and Brendley, 2003). Currently, about 12 million tons of CFAs in the U.S. are utilized in concretes and mortars each year, as SCM or as replacement of fine aggregate. Other applications of CFAs include road sub-base improvement (Del Valle-Zermeño et al. 2014), removal of organic and inorganic elements (Ahmaruzzaman, 2010), etc.

Extensive studies have focused on the beneficial use of CFAs as partial replacement of cement in mortars or concretes (Erdoğdu and Türker, 1998; Aydın et al. 2007; Singhal et al. 2008; Cheerarot and Jaturapitakkul, 2004; Cruz-Yusta et al. 2011; Yüksel et al. 2007;

Reijnders, 2007; Sarıdemir, 2014), in the effort of reducing the environmental footprint and embodied energy of concrete materials while removing CFAs from the waste stream. The chemical composition of CFAs and ordinary Portland cement is similar, but CFAs contain higher silica content and ordinary Portland cement contains higher lime content (Ramezanianpour, 2014). Many states have allowed the use of performance-specified (ASTM C1157) cements that contain CFA. The physico-chemical properties of CFAs can vary significantly across power plants, due to differences in the raw materials and in the burning processes (Bilodeau et al. 1994; Ma, et al. 1999). Traditionally CFAs have been divided into two primary classes, F and C, following the provisions of ASTM C618. Additional characteristics of importance include the calcium oxide content, fineness, crystalline structure, and loss-on-ignition or LOI (mainly an indicator of free carbon content) of the ash (Malvar and Lenke, 2006; Du et al. 2012).

The last decade has seen the complete replacement of cement by CFAs in mortars or concretes to garner considerable interest. The vast majority of studies in this field have focused on alkali activated binder materials such as geopolymer and alkali activated fly ash (del Valle-Zermeño et al. 2014; Duxson et al. 2007 and 2015; Oh et al. 2012; McLellan et al. 2011; Habert et al. 2011; Reddy et al. 2012; Gartner, 2004; Shi et al. 2005; Yost et al. 2013a and 2013b). These cementitious binders are typically activated by hydroxides of alkali elements, such as Li, Na, and K (del Valle-Zermeño et al. 2014; Xie et al. 2010; Roy et al. 1995; Shi et al. 1996). Such addition provides a high pH environment to promote the reactions between the alkali metals or alkali-earth metals, silicates, and aluminates to form the cementitious gel. The preparation of these binders requires specific curing conditions such as pre-treatment of the CFA, relatively high curing temperature, or high pH (Palomo et al. 1999; Guerrero et al. 2004; Bakharev 2005; Goñi and Guerrero, 2007), which has hindered their applications in the construction industry.

Novel uses of CFAs as cementitious binder can produce cost and energy savings and reduce greenhouse gas emissions and landfill waste. This work reports an environmentally friendly cementitious binder material made from only the pure class C coal fly ash (received from supplier without further treatment), water, and a very small amount of borax ($Na_2B_4O_7$), at room temperature and without direct alkali activation. The use of borax in this system was originally intended to mitigate the "flash set" phenomenon observed in this low water/fly ash ratio paste. However, further investigation detailed in this work implies its multifunctional role. In addition to serving as a set retarder, borax may serve as a chemical activator, with its Na^+ cations and $B_4O_7^-$ anions both participate in the formation of hydration products. Such implementation of CFAs as the sole binder in concretes and mortars would translate to even greater environmental and economic benefits, relative to the use of CFAs as SCM or their use in geopolymer and alkali activated fly ash. Previous studies have demonstrated the feasibility of using selected CFAs as the sole binder for structural concrete and reported macro-scale engineering properties of this type of "green" concrete material (Roskos et al. 2011; Cross et al. 2008 and 2010). Nonetheless, mechanisms underlying the properties of this unconventional cementitious binder remain unclear, and this lack of understanding makes it difficult to transfer such technology to CFAs with similar or different physico-chemical characteristics. In this context, this work is devoted to elucidating the hydration process and hydration mechanisms of this "green" cementitious binder, pure fly ash paste (PFAP), using ordinary Portland cement paste (OPCP) as control.

CHAPTER 3. METHODOLOGY

3.1 Materials Preparation

The CFA was obtained from the Corette electric power plant in Billings, MT, USA and was used to prepare the PFAP without further treatment. An ASTM specification C150-07 Type I/II low-alkali Portland cement (ASH Grove Cement Company, Clancy, MT) was used in this study. The chemical composition of the as-received CFA and the Portland cement were obtained using PANalitical AXIOS PW4400 X-Ray Fluorescence (XRF), with the results shown in Table 3- 1. It can be seen that the fly ash used in this study can be defined as "High Calcium" fly ash or class C fly ash since the CaO content is higher than 25%.

Table 3- 1. Chemical composition of the fly ash and cement (wt.%).

Component	Coal Fly Ash	Cement
SiO_2	29.5	20.4
Al_2O_3	17.3	3.7
Fe_2O_3	6.5	3.4
SO_3	3.5	2.6
CaO	30.6	63.3
P_2O_5	1.3	-
Na_2O	3.1	0.1
K_2O	0.4	0.4
MgO	5.3	3.2
TiO_2	1.6	-
LOI	0.23	2.7

The mix design for the PFAP samples (Table 3- 2) consisted of only fly ash, a very small amount of borax, and water. The water/binder ratio of 0.20 was determined based on extensive trial and error, in order to achieve reasonable workability of fresh paste and reasonable strength of hardened paste. This differed greatly from the water/binder ratio of 0.40 for the OPCP. The workability of the PFAP was tested according to ASTM-C1437, and the workability of the OPCP with water/cement ratio of 0.40 was also tested for comparison.

Table 3- 2. Mix design of the pure fly ash paste and the ordinary Portland cement paste.

Mix design parameter	Ordinary Portland cement paste	Pure fly ash paste
Water/binder ratio	0.40	0.20
Borax (wt.% of fly ash)	-	0.20
Fly ash content	-	100%
Cement content	100%	-

For PFAP sample preparation, the borax was dissolved in the water before the water was mixed with the fly ash. After mixing, the fresh paste was cast into polyvinyl chloride (PVC) molds to form Φ 50.8 mm (diameter) $\times$ 101.6 mm (length) cylinders, and was carefully compacted to minimize the amount of entrapped air. The paste specimens were de-molded after 24 h at room temperature, and then cured in a wet chamber (20 $\pm$ 2°C, relative humidity: 95%) for additional days. To halt the hydration of paste samples at the given age (1, 3, 7, or 28 days), the samples were immersed in acetone for 12 h to remove the free water within them. The compressive strength test followed ASTM C109 and the loading rate was 0.5 mm/min. The average measurement from 6 samples was used as the final data value. The bulk density is only used as a basic property of the PFAP. This was calculated by dividing the weight of PFAP cylinders by its volume.

3.2 Properties Testing

The gas permeability test was performed using liquid methanol as the gas source to determine the gas transport properties of 28-d cured paste specimens. A 10 mm thick specimen was cut from a Φ 50.8 mm (diameter) $\times$ 101.6 mm (length) paste cylinder sample and then oven-dried at 105 ℃ for 24 hours to remove the moisture within the specimen. Subsequently, liquid methanol was added before the specimen was placed and sealed on the top of a cell with a silicone sealant to avoid any leakage of methanol vapor. The initial weight of the whole specimen setup (cell, methanol liquid, and specimen and silicone sealant) was measured at the beginning of the test. The values of mass variation versus time due to the vaporization of methanol liquid at a constant 40 ℃ water bath temperature during the test were continuously recorded at each time interval until a steady-state mass loss was reached. The gas permeability coefficient k (m2/s) was then calculated using these mass variation values (Yang et al. 2011).

The chloride anion (Cl-) permeability of water-saturated, 28-d cured paste specimens was tested via electromigration experiments on a setup featuring a disc-shaped specimen that separated the Cl- source (a solution of 3% NaCl and 1% NaOH) and the Cl- destination (a solution of 1% NaOH). Each compartment contained a clean, 316L stainless steel mesh electrode with similar exposed surface area (~15 cm^2) that was connected to a DC power source. Once the specimen, electrolytes, and electrodes were in place, a 30-volt DC electric field was maintained across the 10 mm thick disc. Chloride concentrations in the destination solution were measured at predetermined time intervals using a chloride sensor that consisted of a custom-made Ag/AgCl electrode and a saturated Calomel electrode (SCE) reference electrode. The chloride sensor was periodically calibrated so that its open circuit potential (OCP) measurements could be converted to units of molarity and plotted as a function of time;

the time of chloride penetration was used in the calculation of apparent chloride diffusion

coefficient, D (m^2/s) (Yang et al. 2009).

At the beginning of the electromigration test, the Gamry Reference 600TM

Potentiostat/Galvanostat/ZRA instrument was employed to measure electrochemical

impedance spectroscopy (EIS) data in order to characterize the microstructural properties of

water-saturated paste specimens. To this end, a platinum mesh was placed in the cathodic

compartment to serve as the counter electrode, whereas the stainless steel electrode and the

SCE in the anodic compartment served as the working electrode and the reference electrode,

respectively. The EIS measurements were taken by polarizing the working electrode at ±10

mV around its OCP, using sinusoidal perturbations with a frequency between 5 mHz and 50

KHz (10 points per decade). The Gamry Echem Analyst TM software was used to plot and fit

the EIS data.

3.3 Microstructure Characterization Methods

The surface morphology of the paste specimens was observed by scanning electron

microscopy (SEM), performed on an FEI-Quanta 200F scanning electron microscope. SEM

was conducted under an accelerating voltage of typically 20 kV. For Energy Dispersive

Spectrometer (EDS), a micro-analytical unit was employed to detect the small variations in

trace element content, using an accelerating voltage of typically 15-20 kV and a scan time of

60 s per sampling area.

Nano-indentation was employed to characterize the hardness and modulus of the plate

specimens. It was performed following the continuous stiffness measurement (CSM) method

with a Nano Indenter XP from American MTS Corporation. Hardness is defined as the ratio

of the load to the projected contact area, H = P/A. The experiments were conducted on the

original, unpolished surface with a ball-on-disk tester of type WTM-2E. The micro-nano

mechanical properties were obtained from the analyses of load-displacement data. In this

study, the loading definition was 50 nN, and the displacement was 0.1 nm. Twenty five indentations were performed on each sample. The indentations were made with 20 m spacing in each indented location. Loading was applied linearly for 10 s, the maximal load was then maintained for 5 s, and unloading occurred over another 10 s.

The thermal properties of the paste powder samples were characterized by differential scanning calorimetry (DSC) and thermogravimetric analyses (TGA), using a Mettler Toledo-TGA/SDTA851[e]. The 28-d paste samples were finely crushed, oven-dried at 105°C for 24 hours, cooled in a desiccator, and weighed before their TG/DSC test. The measurements were performed in air with a temperature range from 25 ℃ to 900 ℃ and a heating rate of 15 ℃/min.

X-ray diffraction (XRD) patterns of the paste specimens were obtained on a Rigaku D/max-rA X-ray diffractometer with Cu Kα radiation ($\lambda = 1.5406$ Å).

3.4 Microstructures of Raw Materials by SEM/EDS/XRD

The analysis of the raw materials (especially the pure CFA) is essential for this work, considering the substantial variations inherent in the physico-chemical characteristics of CFAs from various sources and processes. CFAs can be characterized by different methods to determine their phase, mineral morphology, and chemical composition. These include SEM/EDS for morphology and chemical analyses (Kutchko and Kim, 2006), X-ray diffractometry for phase determination (Ward and French, 2006), differential thermal and thermogravimetric analyses (Paya et al. 1998), and Mössbauer and infrared spectroscopy for intrinsic microstructure analysis (Gomes et al. 1999; Veranth et al. 2000).

Figure 3- 1 illustrates the low and high magnification SEM micrographs of the coal fly ash particles used in this study. As can be seen from Figure 3- 1(a), the vast majority of the CFA particles feature a typical spherical shape with a wide size distribution from micrometers to nanometers and rough surfaces. Due to their high surface energy, the nano

sized CFA particles are apt to form agglomerates or adsorbed on the surfaces of the large particles, as demonstrated in Figure 3- 1(b). There are also some non-spherical particles and other minerals present in the CFA (Figure 3- 2). The chemical analysis of the CFA spheres was enabled by combining SEM with EDS, and the typical results are shown in Figure 3- 3. In addition to elements O and Ca, the spheres were found to contain significant levels of C, Al, Si, Mg, Na, and Fe, and trace amounts of S, P, Ti, and Sr.
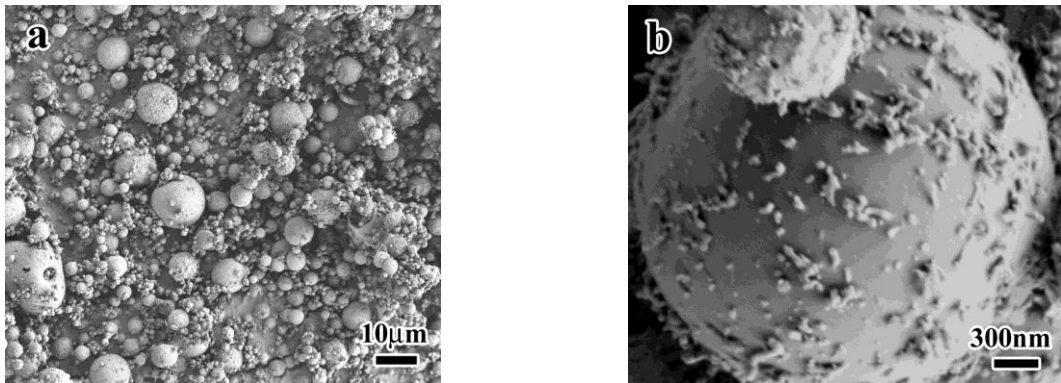
Figure 3- 1. Low and high magnification SEM micrographs of the CFA spheres.
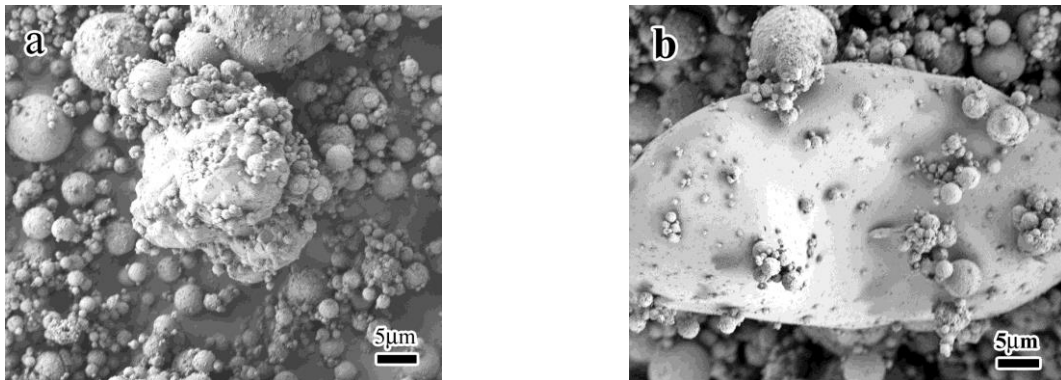
Figure 3- 2. SEM morphologies of the non-spherical fly ash particles.

Element	Wt%	At%
O	63.68	73.33
Na	1.85	1.48
Mg	2.59	1.97
Al	4.04	2.76
Si	4.00	2.62
P	0.67	0.40
S	0.90	0.52
Ca	10.56	4.85
Ti	0.93	0.36
Fe	2.62	0.86
Sr	1.25	0.26
C	6.90	10.58
Total	100.00	100.00
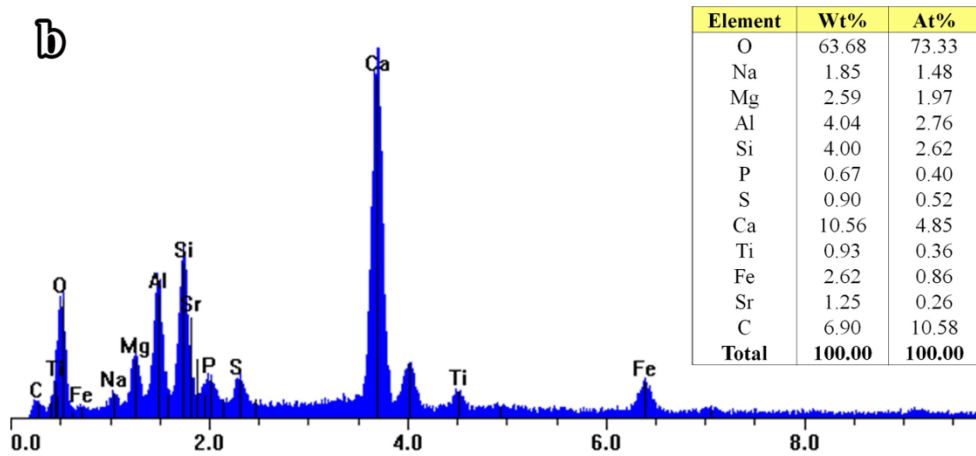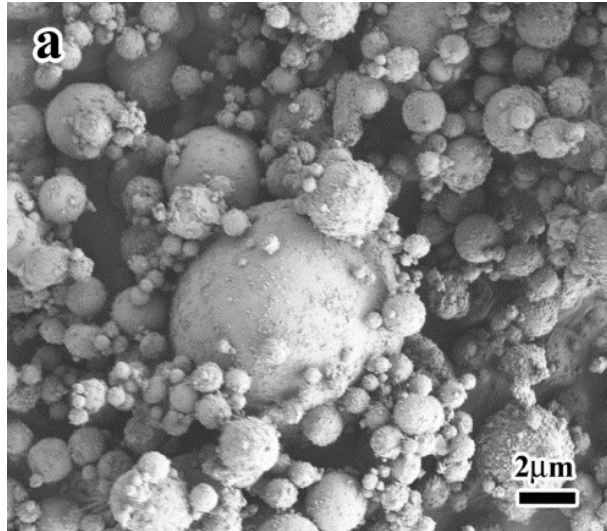
Figure 3- 3. SEM/EDS analysis of the fly ash particles.

The crystalline phases of the coal fly ash were determined by XRD analysis, shown in

Figure 3- 4. As seen in this pattern, the two main peaks appear at about 27 ° and 34 °, which

represent the relatively high content of quartz (SiO_2) and hematite (Fe_2O_3), respectively.

Meanwhile, the peaks of lime (CaO) were also detected at about 38 °, 54 °, and 68 °, and peaks

of periclase (MgO) and alumina (Al_2O_3) were observed as well.
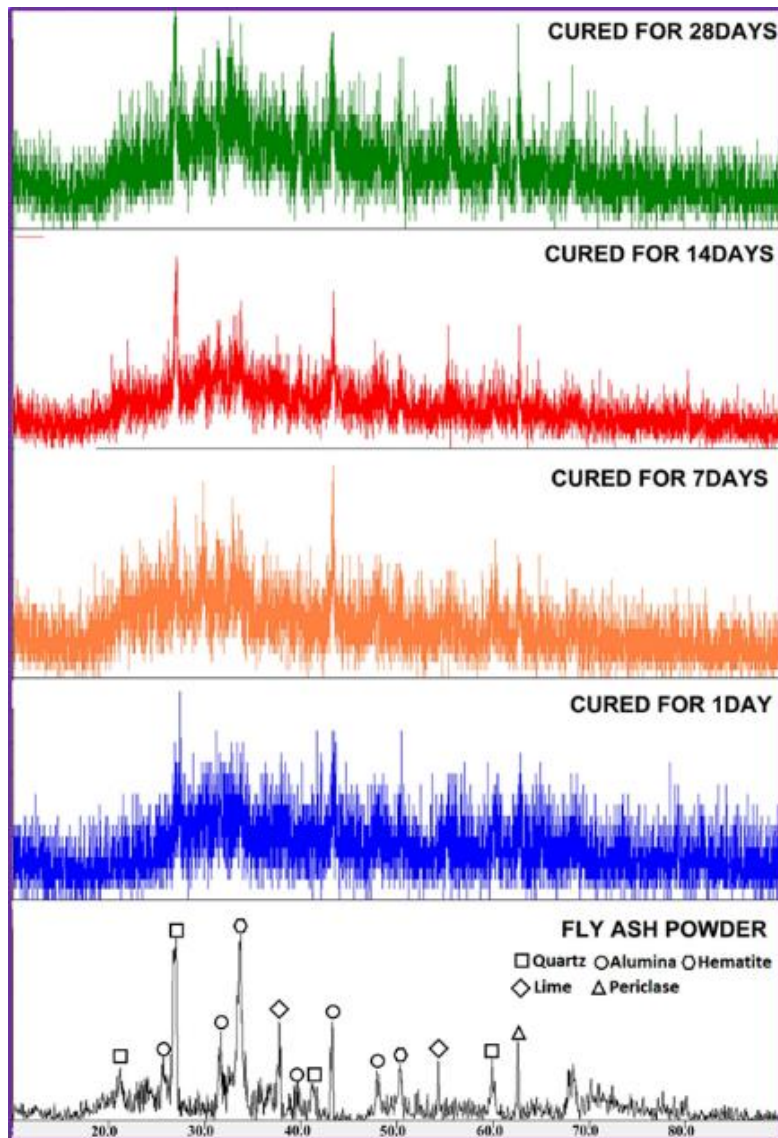
Figure 3- 4. XRD pattern of fly ash powder and PFAP cured for 1,7, 14, and 28 days.

Other studies have revealed that class F CFAs tend to contain mainly crystalline phases of aluminum silicates with iron oxides on the surfaces and some amorphous phases (Kutchko and Kim, 2006; Gomes et al. 1999). For the class C CFA used in this study, however, the combined XRF, SEM/EDS and XRD data suggest that it contains mainly amorphous Al-rich and Ca-rich phases with some crystalline phases of quartz, hematite, free lime, periclase, and alumina.

CHAPTER 4. PROPERTIES AND MICROSTRUCTURES

4.1 Properties of Hardened Pastes

Figure 4- 1 shows the evolution of compressive strength of PFAP as a function of curing time. The PFAP's compressive strength increased logarithmically with curing time, and reached about 36 MPa after 28 days of curing. This value is comparable with the 28d compressive strength of the Portland cement paste (usually varied from 30 to 50 MPa according to different cement types or water/cement ratio). This implies the suitability of this unconventional "green" binder for a host of structural and non-structural concrete applications, without the need for external heating or chemical activation. This binder also features relatively high early-age strengths, which are desirable for accelerated construction and rapid renewal of concrete infrastructure. The compressive strength of the PFAP reached about 19 MPa and 31 MPa after one day and three days of curing, respectively; which means, the 1d and 3d compressive strength have reached the 53% and 86% of the 28d strength. The compressive strength behavior of the pure fly ash pastes is consistent with that of the pure fly ash concretes reported earlier, which generally featured 20 MPa, 33 MPa, and 55 MPa at the age of 1d, 28d, and one year, respectively (Cross and Stephens, 2008).
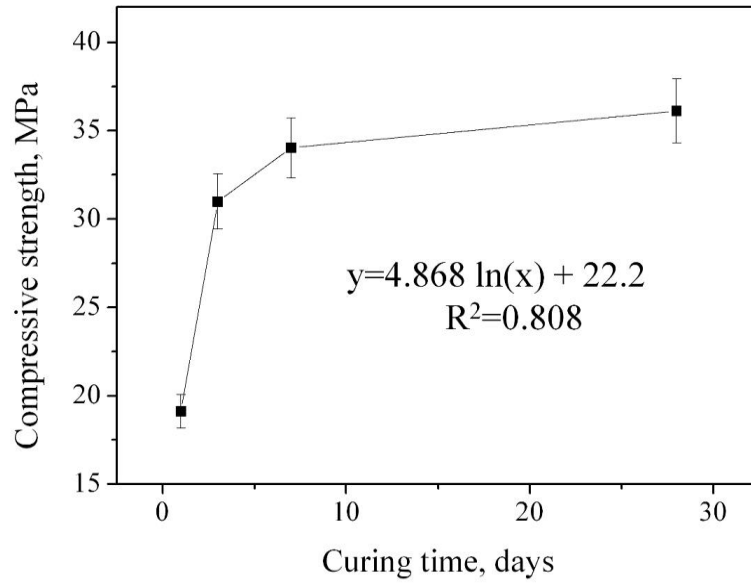
Figure 4- 1. Compressive strength of the PFAP cured for 1, 3, 7, and 28 days.

As shown in Table 4- 1, the PFAP samples show a relatively lower (but still reasonable)

workability with slump of about 121 mm than the OPCP samples with slump of about 216

mm. If needed, such difference in slump values can be readily addressed by the use of high

range water reducer. The PFAP samples featured an average bulk dry density of 1.6 g/cm^3,

which is 20% less than that of the OPCP samples and makes the PFAP a desirable binder in

many applications such as lightweight concrete and concrete fill for hydraulic fracking

operations.

Table 4- 1. Properties of the pure fly ash paste and ordinary Portland cement paste.

Properties	ordinary Portland cement paste	pure fly ash paste
Slump	216 mm	121 mm
28-d Compressive strength (MPa)	56	36
Bulk Dry Density (g/cm^3)	2.0	1.6
Surface Resistivity (kΩ·cm)	6.2	1.3×10^2
Bulk Resistivity (kΩ·cm)	12	1.5×10^4
Hardness, H (GPa)	1.4	1.8
Elastic Modulus (GPa)	37.6	39.4
Gas permeability coefficient, k (10^{-17} m^2/s)	4.8	4.1
Chloride diffusion coefficient, D (10^{-12} m^2/s)	1.5	1.9
Q (S/cm^2)	217	147
R (kΩ.cm^2)	35	154

Furthermore, Table 4- 1 shows that the PFAP samples featured an average surface (electrical) resistivity of 1.3×10^2 kΩ·cm and an average bulk resistivity of 1.5×10^4 kΩ cm, which are considerably higher than those of the OPCP samples. This may be attributable to lower conductivity of hydration products in the paste bulk, lower amount of ions in the pore solution of the PFAP, lower porosity, and/or lower amount of percolated pores in the PFAP (Rajabipour and Weiss, 2007).

Table 4- 1 also lists the hardness and elastic modulus, gas permeability coefficient, Cl⁻ diffusion coefficient, and electrochemical parameters of the PFAP, in comparison with the

OPCP. The nano-indentation test results show that the average micro-nano hardness and elastic modulus of PFAP were 1.8 GPa and 39.4 GPa, respectively. These are 29% and 5% higher than those of the OPCP (1.4 GPa and 37.6 GPa), respectively. The average gas permeability coefficient of the PFAP was 4.1×10^{-17} m^2/s, which is about 15% lower than the OPCP. However, the average Cl$^-$ diffusion coefficient of the PFAP was 1.9×10^{-12} m^2/s, which is 27% higher than that of the OPCP. Such inconsistent differences in the relative performance of PFAP and OPCP can be explained by the different percolation pathways by gas and liquid in porous media. Relative to the OPCP, the PFAP samples have a higher amount of confined water (as indicated by the DSC data discussed later), which offers more critical paths for liquid transport while decreasing the gas penetration. Another complicating factor is the chloride binder capacity of these pastes, which plays a significant role in the diffusion of free chloride as well.

The EIS parameters that characterize the electrolyte–paste interface are the ionic transport resistance (R) and the capacitance (in this case, constant phase element) of the paste disc (Q). Relative to the OPCP, the PFAP samples featured much greater R (154 vs. 35 kΩ.cm^2) and significantly lower Q (147 vs. 217 S/cm^2). The higher ionic transport resistance and lower electric capacitance of PFAP suggest a denser microstructure, relative to the OPCP. Note that this finer microstructure factor contributed to lower gas permeability, higher electrical resistivity, and higher micro-nano hardness, but is overshadowed by other factors in the case of chloride permeability or compressive strength.

4.2 Characterization of the PFAP

XRD of the pastes at different ages

XRD was employed for the phase determination of the cementitious materials, and the

results suggest some potential mechanisms of the hydration reaction of the PFAP (Baur and

Johnson, 2003; Johnson and Kersten, 1999). Figure 3- 4 shows the XRD pattern of the fly ash

powders and the PFAP cured for 1d, 7d, 14d, and 28d, respectively. As can be seen in this

figure, a few crystalline phases can be observed in the fly ash powders, including quartz

(SiO_2) alumina (Al_2O_3), hematite (Fe_2O_3), periclase (MgO), and lime (CaO). This is well

agreed with the XRF results demonstrated in Table 3- 1. As illustrated in this figure, the

PFAP features a predominantly amorphous structure. However, similar to C-S-H phases in

hydrated Portland cement, some small size non-reacted crystalline phases remain in the

hydration products and their quantification is a big challenge. By comparing with the as-

received fly ash powder, it can be seen that a few unreacted phases of quartz, alumina,

periclase and hematite remain in the hydrated fly ash paste.

The diffraction patterns share similar phase compositions, but the peaks show different

intensities as a function of curing time. In this figure, the main characteristic peaks of the

alumina hydrate appear at about 27 °and 43 °, and they keep increasing with longer curing

time, until 14 days, which demonstrates the increasing quantity of the alumina hydrate

crystals. These peaks in the 28 d samples become lower and wider, implying the dissolution

and size reduction of the alumina hydrate crystals. The main peaks of the hematite and

periclase phases appear at about 33 °and 63 °, respectively, and their intensity evolution with

curing time was similar to that of aluminum hydroxide phases. The detailed composition of

the PFAP amorphous phases is hard to determine using XRD alone; as such, they should be

analyzed using a combination of other characterization techniques in future research.

SEM/EDS of the hardened pastes

The low magnification fracture surface SEM micrographs of the PFAP cured for 1, 7, 14,

and 28 days are shown in Figure 4- 2. It can be observed from this figure that the microscopic

fracture of the PFAP mainly occurred on the hydration products or the interfaces between

them and the fly ash spheres. In other words, fracture on the fly ash spheres rarely occurred.

After curing for 1 day (Figure 4- 2(a)), at the beginning of the hydration reaction, many

micro-cracks and micro-pores were found, and at the surfaces of the fly ash spheres, small

unreacted particles were observed. Due to the incomplete hydration reaction, the interfaces

between the fly ash spheres and the hydration products were not very obvious, and pits were

rarely observed at the fracture surface. After curing for 7 days (Figure 4- 2(b)), with the

progress of the hydration reaction, more hydration products with higher densities were

observed. However, the surfaces of the fly ash spheres were still not very smooth, and many

unreacted small particles were observed as well, in addition to some pits. This demonstrates

that the cracks were propagated not only from the hydration products themselves, but also

from the interfaces between the fly ash spheres and the hydration products. After curing for

14 days (Figure 4- 2(c)), the morphology of the fracture surface was considerably different

from those cured for only 1 day or 7 days. The number of unreacted small particles on the fly

ash spheres decreased significantly, the interfaces between the fly ash spheres and the

23

hydration products became smoother, the hydration products became much denser, the quantity of micro-cracks and micro-pores decreased significantly, and the quantity of pits increased. The observed morphology suggests that the quantity of hydration products increased with curing time, and that the interfaces between them and the fly ash spheres became another type of defects inside the PFAP matrix. After curing for 28 days (Figure 4-2(d)), with much of the hydration process completed, the microscopic fracture surface of the PFAP became relatively clear and consisted of only the pits, amorphous glassy phases, and spherical fly ash particles. The surfaces of the fly ash spheres were smooth, and few unreacted particles were observed, although some air voids and micro-cracks were still visible.
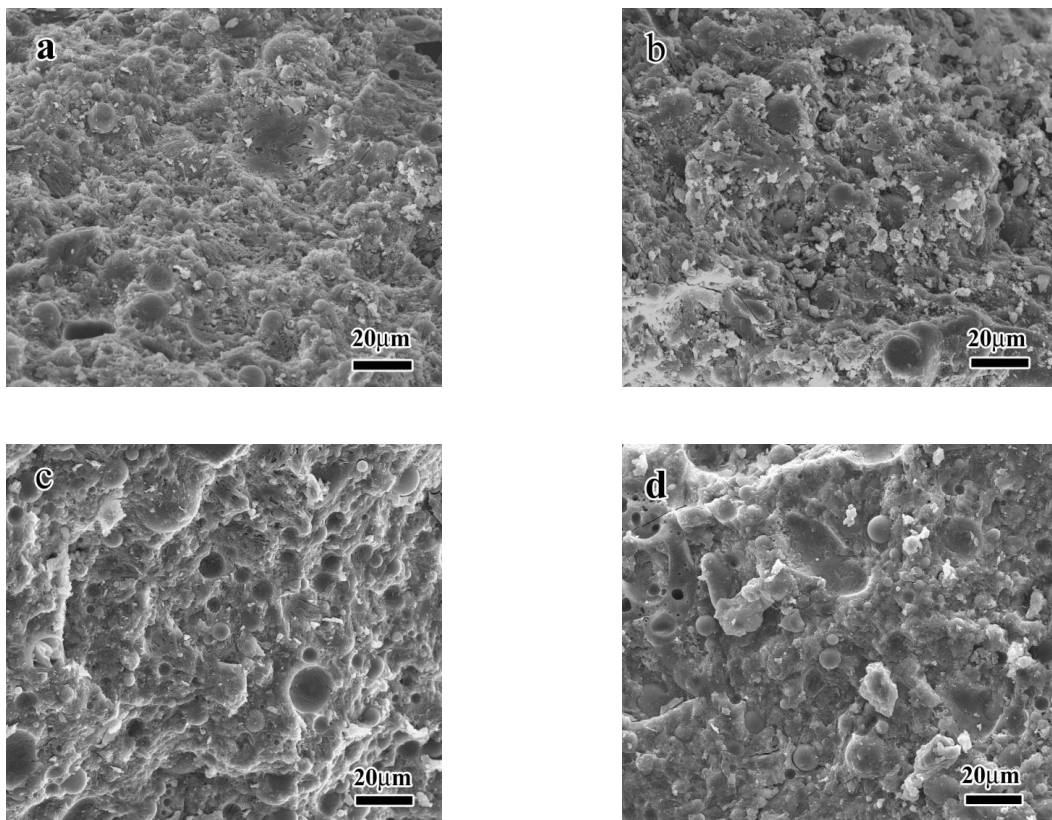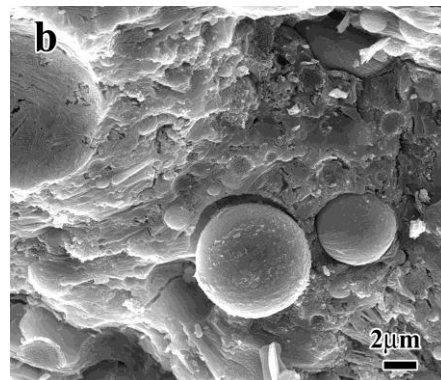

Figure 4- 2. Low magnification SEM micrographs of the fracture surfaces of PFAP cured for a) 1 day, b) 7days, c) 14 days, d) 28 days

The high magnification fracture surface SEM micrographs of the PFAP cured for 1, 7,

14, and 28 days are shown in Figure 4- 3, and Figure 4- 4 gives the SEM/EDS results of the

PFAP fracture surface cured for 28d. As can be seen from Figure 4- 3, the cured PFAP can be

divided into two main types, unreacted fly ash spheres and hydration products. It can be seen

from Figure 4- 4 that the chemical composition of the unreacted fly ash spheres mainly

consists of Al, Si, Ca, Na, Mg, and Fe. Figure 4- 5 and Figure 4- 6 show the fracture surface

SEM images and the corresponding EDS results in various areas cured at 1d and 28d,

respectively. At the beginning of the hydration process (cured for 1day), the microscopic

areas with higher Si or Ca content show smoother surfaces than those with higher Mg or Fe

content. In the fly ash spheres, the ratios between the Mg/Fe/Al/Si/Ca could be 1:3:2:1.5:6

(Figure 4- 5, area 1), or 1:1.5:0.5:0.3:5 (Figure 4- 5, area 3). After curing for 28 days, the

same ratios in the fly ash spheres developed to about 1:1:2:2:2.5 (Figure 4- 6, area 7). This

reveals marked decrease in the Ca/Si and Fe/Si ratios and significant decrease in the Al/Si

and Mg/Si ratios, likely due to the dissolution of Ca-rich, Fe-rich and Al-rich phases and the

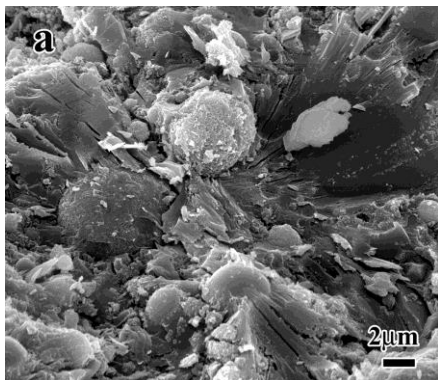subsequent consumption of Ca^{2+}, Fe^{3+}, Al^{3+} and Mg^{2+} by the hydration reactions.
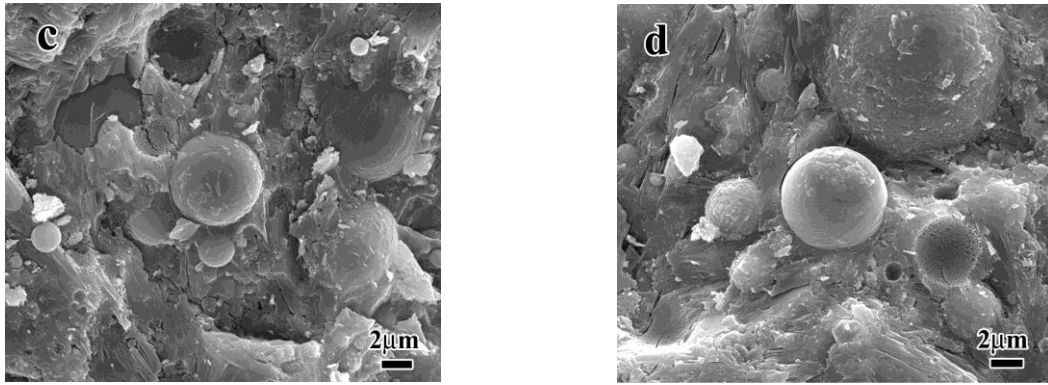
Figure 4- 3. High magnification SEM micrographs of the fracture surfaces of PFAP cured for a) 1 day, b) 7days, c) 14 days, d) 28 days

Element	Wt%	At%
CK	08.56	15.29
OK	35.63	47.79
NaK	01.64	01.53
MgK	04.26	03.76
AlK	08.77	06.97
SiK	14.16	10.82
SK	01.48	00.99
ClK	00.20	00.12
KK	00.27	00.15
CaK	19.04	10.19
TiK	01.21	00.54
FeK	04.79	01.84
Matrix	Correction	ZAF

Figure 4- 4. The SEM/EDS images of PFAP cured for 28 day

Unlike the fly ash spheres, the hydration product morphology of the PFAP was similar

to that of the Portland cement, featuring a lamellar shape and similar chemical compositions.

26

As seen from the EDS data, at the beginning of the hydration process, the ratios of Mg/Fe/Al/Si/Ca were 1:1:1:7:7 (Figure 4- 5, area 2) for the lamellar hydration products. The ratios developed to 1:2:4:2:9 after curing for 28 days (Figure 4- 6, area 8). This reveals marked increase in the Al/Si, Fe/Si, Ca/Si, and Mg/Si ratios, due to the uptake of Al^{3+}, Fe^{3+}, Ca^{2+}, and Mg^{2+} from fly ash spheres.

Element	Wt%	At%
CK	04.47	11.85
OK	19.80	39.41
NaK	00.59	00.82
MgK	09.19	12.03
AlK	07.01	08.27
SiK	04.53	05.14
SK	01.17	01.16
KK	00.14	00.11
CaK	17.04	13.54
TiK	00.88	00.59
FeK	03.42	01.95
AuL	31.76	05.13
Matrix	Correction	ZAF

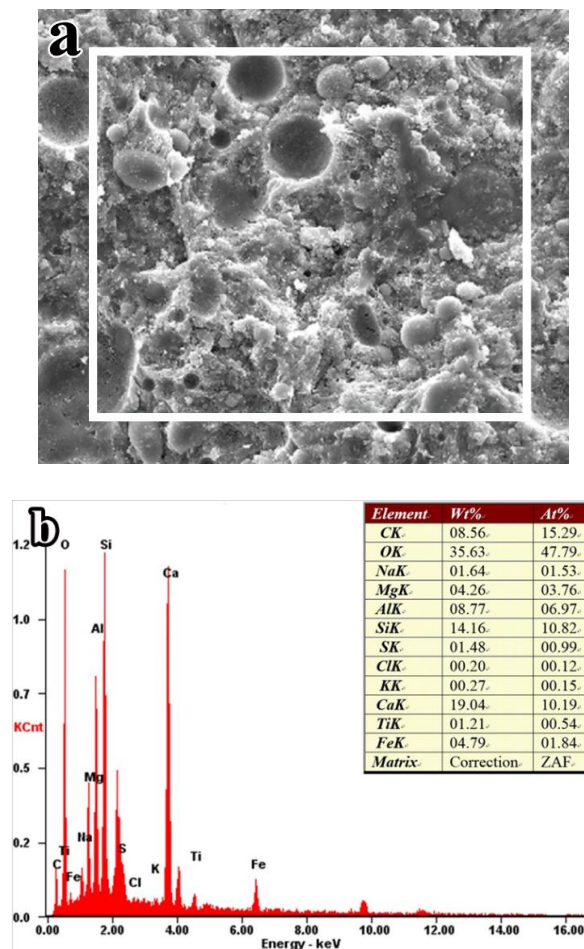| Element	Wt%	At%
CK	11.91	27.39
OK	13.45	23.22
NaK	01.39	01.67
MgK	03.41	03.87
AlK	03.59	03.68
SiK	21.46	21.11
SK	00.30	00.25
KK	00.28	00.20
CaK	19.50	13.44
TiK	01.03	00.59
FeK	03.54	01.75
AuL	20.14	02.82
Matrix	Correction	ZAF

Element	Wt%	At%
CK	01.91	06.29
OK	12.98	32.13
NaK	00.00	00.00
MgK	06.19	10.08
AlK	02.70	03.96
SiK	01.87	02.63
SK	00.41	00.50
KK	00.27	00.28
CaK	29.50	29.14
TiK	01.35	01.12
FeK	10.40	07.37
AuL	32.43	06.52
Matrix	Correction	ZAF

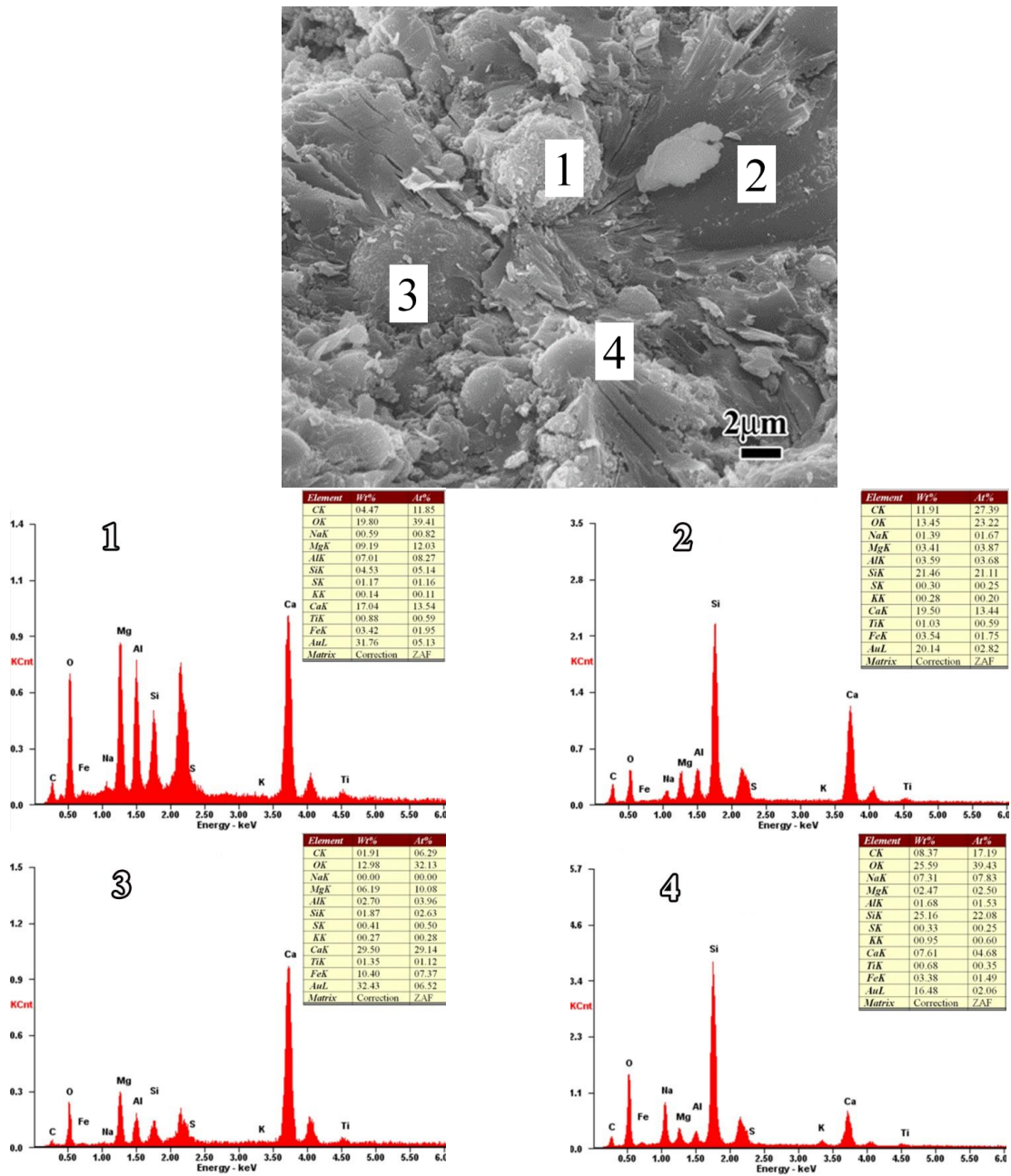| Element	Wt%	At%
CK	08.37	17.19
OK	25.59	39.43
NaK	07.31	07.83
MgK	02.47	02.50
AlK	01.68	01.53
SiK	25.16	22.08
SK	00.33	00.25
KK	00.95	00.60
CaK	07.61	04.68
TiK	00.68	00.35
FeK	03.38	01.49
AuL	16.48	02.06
Matrix	Correction	ZAF

Figure 4- 5. The fracture surface EDS results of PFAP at various areas cured for 1 day
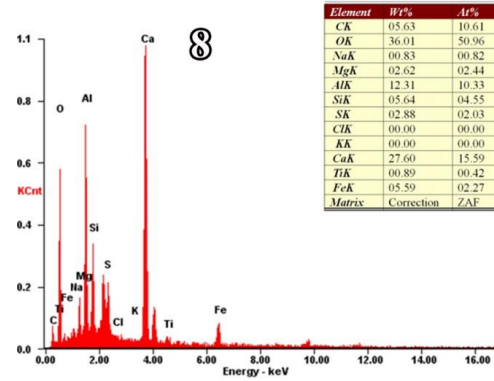
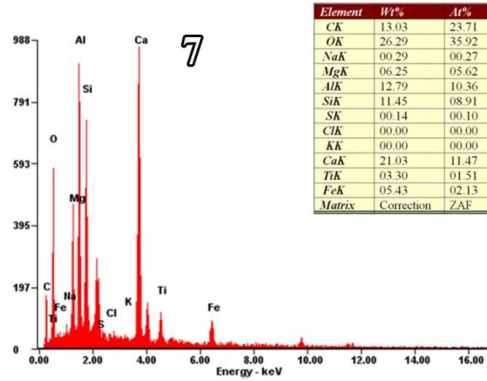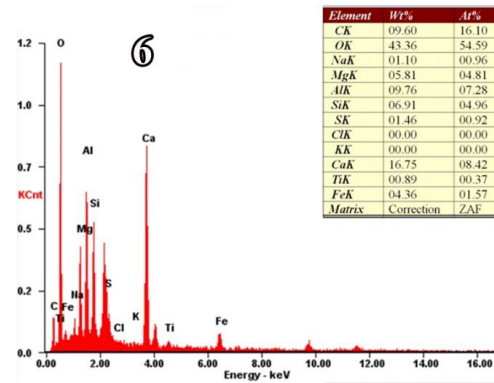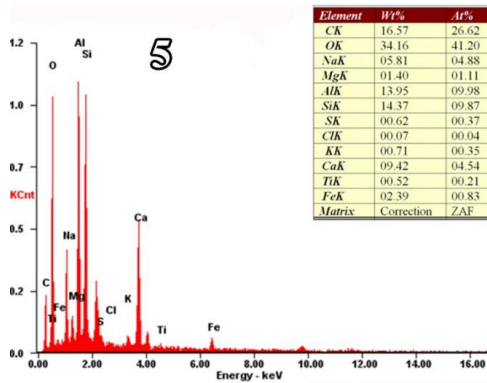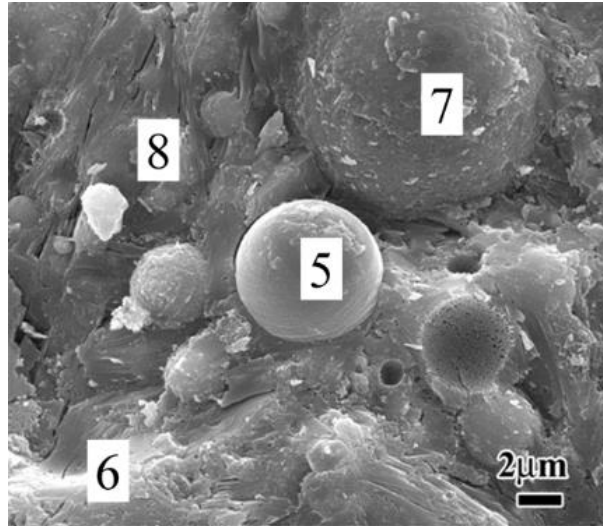**Figure 4- 6. The fracture surface EDS results of PFAP at various areas cured for 28 days**

DSC/TGA of the hardened pastes

The DSC/TGA curves have been widely used to identify the phases of hydration

products of cementitious materials (Pelisser et al. 2012). The DSC thermogram illustrates the

heat flow between the hardened paste powder sample as a function of temperature, and the

TGA pattern shows the weight loss of the sample as a function of temperature.

The DSC thermogram of PFAP and OPCP is presented in Figure 4- 7(a), and there is

marked difference between the two. Figure 4- 7(a) reveals that the OPCP thermogram

features three major variations during the heating process. The first one, attributed to the

dehydration of the water confined in the hydration products of Portland cement paste, started

at about 90 ℃ and ended around 100 ℃. The second major peak started from about 425 ℃ and

ended around 475 ℃, corresponding to the decomposition of Portlandite (calcium hydroxide).

The third variation started at about 650 ℃ and ended around 675 ℃, corresponding to the

decomposition of the calcium carbonate. Figure 4- 7(a) reveals that the PFAP thermogram

features one major variation during the heating process. While this peak also started at about

90 ℃ and ended around 200 ℃. In light of the higher Al_2O_3 content in the raw material, the

wider shoulder in this thermogram may be attributed to the decomposition of alumina hydrate

and ettringite phases (e.g., $4CaO \cdot Al_2O_3 \cdot SO_3 \cdot 12H_2O$) (Chakraborty et al. 2013). Unlike the

OPCP, the PFAP did not exhibit any obvious Portlandite decomposition peak. This is partly

due to the lower CaO content in the binder. This also implies that the non-cementitious

Portlandite formed during the hydration of the Class C fly ash was further converted to form

C-S-H or other cementitious phases, which is desirable for strength and durability of the

hardened paste (Feng et al. 2013). A small peak around 250 ℃ to 280 ℃ was detected, which

is attributable to the decomposition of the alumina hydrate phase. Finally, the calcium

carbonate decomposition peak was barely observed in the PFAP thermogram. The low

calcium carbonate content in the PFAP can be attributed to the lower amount of Ca^{2+} cations available for carbonation.

The composition difference between the PFAP and the OPCP was further supported by their marked difference in the thermogravimetric pattern (Figure 4- 7(b)), i.e., TGA. The hardened OPCP exhibited three obvious decreasing slopes at about 90 ℃, 450 ℃, and 650 ℃, respectively, which corroborates the DSC peaks corresponding to confined water dehydration, Portlandite decomposition, and calcium carbonate decomposition. The OPCP featured a mass loss of about 5 % at 100 ℃, another 3% in the range of 425 ℃ to 475 ℃, and another 1.5% in the range of 625 ℃ to 675 ℃. In contrast, the hardened PFAP exhibited one main decreasing slope in the range of 25 ℃ to 200 ℃ (with a mass loss of about 6%), corresponding to the loss of confined water and decomposition of alumina hydrate. The mass loss of the cementitious paste with increasing temperature is mainly the result of water loss from and decomposition of the binder phases. As such, the hardened PFAP exhibited better heat resistance (less mass loss) than the hardened OPCP. This makes the PFAP a desirable binder in many applications such as fire-resistant concrete.

It is worth noting that the hardened PFAP exhibited better heat resistance (less mass loss) than the hardened OPCP, which makes the PFAP a desirable binder in many applications such as fire-resistant concrete.
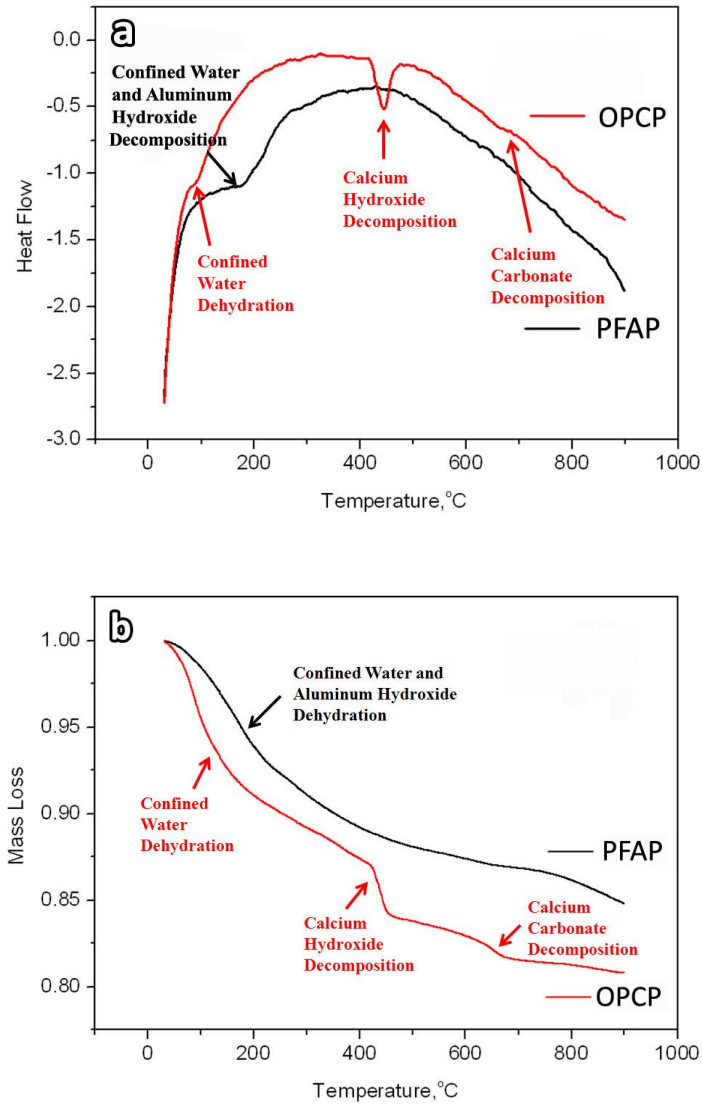
Figure 4- 7. DSC and TGA patterns of PFAP and OPCP after cured for 28 days at room temperature with humidity of 95%. (a) DSC, and (b) TGA

4.3. Hydration Mechanisms for the PFAP

It was found that the C-S-H in hardened Portland cements paste generally has an average

Ca/Si ratio of about 1.75, and varies from about 1.2 to 2.1 (Richardson, 1999). A few

outstanding models demonstrated that the nanostructure of C-S-H is mainly falling into two

types (Allen et al. 2007). One is where the silicate anions are entirely monomeric, and the

other one is where linear silicate chain is present in 1.4 nm tobermorite (and a number of

other minerals) (Taylor, 1986). In addition to the above mentioned model, another solid C-S-H model was developed based on the H_2O/D_2O SANS contrast variation approach. In this model, the nanoscale Portlandite phase can be quantified and the solid C-S-H formula, $(CaO)_x(SiO_2)(H_2O)_y$, are able to be determined in terms of x and y, together with its mass density (Thomas et al. 1998). In general, the main hydration reaction of ordinary Portland cement paste can be written as (Thomas et al. 1998; Taylor and Harry, 1997; Bentz, 1997):

$$C_3S + 5.3H_2O \rightarrow C_{1.7}SH_4 + 1.3CH \tag{1}$$

$$C_2S + 4.3H_2O \rightarrow C_{1.7}SH_4 + 0.3CH \tag{2}$$

or

$$C_3S + zC_2S + wH_2O \rightarrow (1+z)C_xSH_y + pCH \tag{3}$$
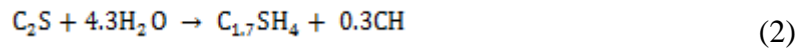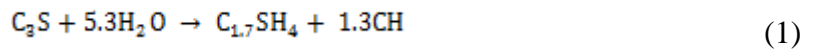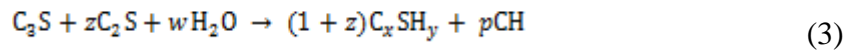
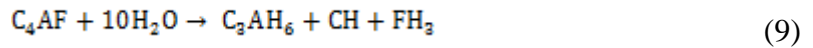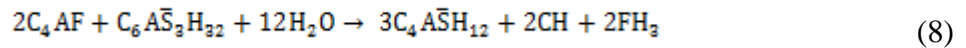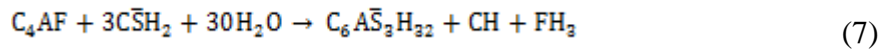With addition of aluminate and ferrite, the reaction will become as:

$$C_3A + 6H \rightarrow C_3AH_6 \tag{4}$$

$$C_3A + 3C\bar{S}H_2 + 26H_2O \rightarrow C_6A\bar{S}_3H_{32} \tag{5}$$

$$2C_3A + C_6A\bar{S}_3H_{32} + 4H_2O \rightarrow 3C_4A\bar{S}H_{12} \tag{6}$$

$$C_4AF + 3C\bar{S}H_2 + 30H_2O \rightarrow C_6A\bar{S}_3H_{32} + CH + FH_3 \tag{7}$$

$$2C_4AF + C_6A\bar{S}_3H_{32} + 12H_2O \rightarrow 3C_4A\bar{S}H_{12} + 2CH + 2FH_3 \tag{8}$$

$$C_4AF + 10H_2O \rightarrow C_3AH_6 + CH + FH_3 \tag{9}$$
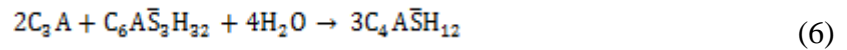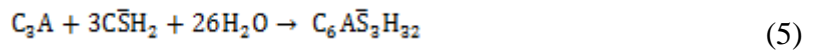
In comparison, the main hydration reactions of PFAP may consist of some additional hydration reactions as follows (Pace et al. 2011):

$$4CaO + 3Al_2O_3 + SO_3 + 18H_2O \rightarrow 4CaO \cdot Al_2O_3 \cdot SO_3 \cdot 12H_2O + 2Al_2O_3 \cdot 6H_2O \tag{10}$$

$$4CaO + 3Al_2O_3 + SO_3 + 2CaSO_4 + 38H_2O \rightarrow 6CaO \cdot Al_2O_3 \cdot 3SO_3 \cdot 32H_2O + 2(Al_2O_3 \cdot 3H_2O) \tag{11}$$

$$4CaO + 3Al_2O_3 + SO_3 + 6CaO + 8CaSO_4 + 96H_2O \rightarrow 3(6CaO \cdot Al_2O_3 \cdot 3SO_3 \cdot 32H_2O) \tag{12}$$
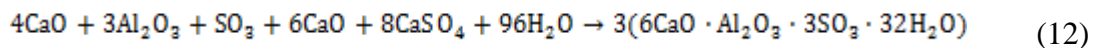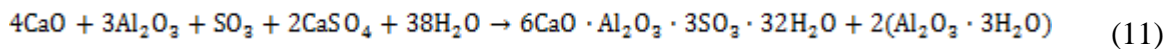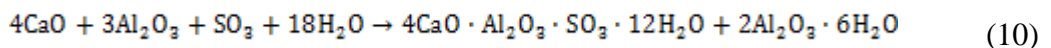
Borax was admixed in the fresh fly ash paste as a set retarder, since the PFAP samples in the absence of borax exhibited the behavior of flash setting. Nonetheless, the role of borax is multifunctional, which merits further investigation. For instance, the incorporation of borax ($Na_2B_4O_7$) also played a significant role in the pH of the pore solution, through the hydrolysis of the borax shown as:

$$Na_2B_4O_7 + 2H_2O \rightarrow 2Na^+ + 2OH^- + H_2B_4O_7 \tag{13}$$
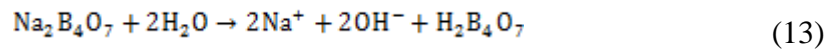
As suggested by the data discussed so far, the hydration of the CFA is very complex and likely entails reactions between the free Ca^{2+}, Fe^{3+}, Al^{3+}, and Mg^{2+} and silicates to form amorphous Al-rich and Fe-rich binder phases and more crystalline binder phases including, alumina hydrate, C-S-H, M-A-S-H, C-A-S-H, etc. The ettringite formation, especially if occurring at a late age of the hardened paste, would introduce undesirable expansive stress inside the paste matrix and pose a risk to its integrity. As such, the SO_3 content in the CFA plays a crucial role in controlling the amount of ettringite in the hardened paste. As shown in Eqn. (13), admixing borax into the fresh paste leads to the formation of boric acid, which can also react with Ca^{2+}, alumina, and water and thus reduce the amount of ettringite formed.

In the hydration process of cement paste, the reaction between the CaO and water occurs very quickly to produce Ca^{2+} and OH^- ions. Under this high pH condition, silicates will dissolve quickly, which then combine the Ca^{2+} cations in the solution to form the main phase of the binder, C-S-H. Different from ordinary Portland cement, fly ash features a higher Al_2O_3 and lower CaO content and thus its hydration products are different. A decrease in the CaO will decrease the concentrations of Ca^{2+} and OH^- ions in the pore solution. As the pore

solution of the PFAP features a pH not as high as that of the OPCP, the dissolution of

silicates in CFAs into the solution typically becomes slower. This helps to explain the

continued strength development of the pure fly ash concretes beyond 28 days and up to one

year (Cross and Stephens, 2008).

The high early-strength of the PFAP samples can be attributed to the fact that this class

C CFA mainly composed of amorphous Al-rich and Ca-rich phases with some crystalline

phases of quartz, hematite, free lime, periclase, and alumina, instead of crystalline phases of

aluminum silicates (in the case of class F CFAs). The significant level of Al and trace amount

of Fe in this CFA may contribute to the hydration process as well, as Goñi claimed that the Si

in the C-S-H chains can be substituted by Al or Fe in a class C CFA belite cement (Goñi and

Guerrero, 2007). Through a Mössbauer spectroscopy study, Lemougna suggests that Fe is

able to play a positive role to form the binder phase in the fly ash cement paste (Lemougna et

al. 2013). The study claimed that the forsterite in the original ashes will not react with OH^-,

but part of the augite phase will be dissolved and form new hydration products.

The high alkali content and low impurity content in the CFA also contributed to the high

early-strength of the PFAP samples. As shown in Table 1, the equivalent alkali content

(expressed as $\%Na_2O + 0.658 \times \%K_2O$) is considerably higher in the CFA (3.4%) than that in

the cement (0.4%), whereas the LOI (mainly an indicator of free carbon content) is

considerably lower in the CFA (0.23%) than that in the cement (2.7%). These characteristics

of the CFA made its hydration behavior to differ from that of typical high-impurity, low-

alkali CFAs.

CHAPTER 5. CONCLUSIONS

(1) This study focused on preparing a novel pure fly ash paste as a potential replacement for the cement paste, in order to reduce the life cycle environmental footprint of cementitious materials. The PFAP was successfully prepared at room temperature with an as-received coal fly ash, borax, and with water/binder ratio of 0.2.

(2) The hardened pure fly ash paste exhibited a reasonable 28-d compressive strength (36 MPa), rapid strength gain (19MPa and 31 MPa in 1d and 3d, respectively), low bulk dry density (1.6 g/cm3), very high electrical resistivity, outstanding micro-nano hardness and elastic modulus, low gas permeability coefficient (4.1×10-17 m2/s), reasonably low Cl- diffusion coefficient (1.9×10-12 m2/s), a denser microstructure, and better heat resistance than the ordinary Portland cement paste. The properties of the PFAP make it a viable "green" construction binder suitable for a host of structural and non-structural applications.

(3) The hydration mechanisms of this "green" binder were presented by characterizing the raw material and PFAP pastes via XRF, SEM/EDS, XRD, and DSC/TGA approaches. The data reveal that the hydration of the CFA is very complex and likely entails reactions between the free Ca^{2+}, Fe^{3+}, Al^{3+}, and Mg^{2+} and silicates to form amorphous Al-rich and Fe-rich binder phases.

(4) While this work only showcases the properties of one specific CFA, the obtained knowledge sheds light on the role of class C CFA in the hydration process and may benefit the expanded use of various CFAs in the manufacturing of paste, mortar, and concrete materials.

REFERENCES

Ahmaruzzaman, M. (2010). "A review on the utilization of fly ash." *Progress in Energy and Combustion Science*, 36 (3), 327-363.

Akkaya, Y.; Ouyang, C.; and Shah, S. P. (2007). "Effect of supplementary cementitious materials on shrinkage and crack development in concrete." *Cement and Concrete Composites,* 29 (2), 117-123.

Allen, A.J.; Thomas, J.J.; and Jennings, H.M. (2007). "Composition and Density of Nanoscale Calcium-Silicate-Hydrate in Cement." *Nature Materials*. 6 (4), 311-316.

Aydın, S., Yazıcı, H., Yiğiter, H., and Baradan, B. (2007). "Sulfuric acid resistance of high-volume fly ash concrete." *Building and Environment*, 42 (2), 717-721.

Bakharev, T. (2005). "Geopolymeric materials prepared using Class F fly ash and elevated temperature curing." *Cement and Concrete Research*, 35 (6), 1224-1232.

Baur, I.; Johnson, C. A. (2003). "Sorption of selenite and selenate to cement minerals." *Environmental Science and Technology*, 37 (15), 3442-3447.

Bentz, D. P. (1997). "Three Dimensional Computer Simulation of Portland Cement Hydration and Microstructure Development." *Journal of the American Ceramic Society*, 80 (1), 3-21.

Bilodeau, A., Sivasundaram, V., Painter, K. E., and Malhotra, V. M. (1994). Durability of concrete incorporating high volumes of fly ash from sources in the USA. ACI Materials Journal, 91(1).

Chakraborty, S.; Kundu, S. P.; Roy, A.; Adhikari, B.; Majumder, S. B. (2013). "Effect of jute as fiber reinforcement controlling the hydration characteristics of cement matrix." *Industrial and Engineering Chemistry Research*, 52 (3), 1252-1260.

Cheerarot, R.; and Jaturapitakkul, C. (2004). "A study of disposed fly ash from landfill to replace Portland cement." *Waste Management*, 2004, 24, 701-709.

Cross, D., Stephens, J., Jones, W., & Leach, L. (2008). Evaluation of the Durability of 100 Percent Fly Ash Concrete. Coal Combustion By-Products Consortium: Morgantown, WV.

Cross, D.; Stephens, J.; and Berry, M. (2010). "Sustainable Construction Contributions from the Treasure State: Research and applications show promise of 100% fly ash concrete." *Concrete International*, 32 (5), 41-46.

Cruz-Yusta, M.; Mármol, I.; Morales, J.; and Sánchez, L. (2011). "Use of olive biomass fly ash in the preparation of environmentally friendly mortars." *Environmental Science and Technology*, 45 (16), 6991-6996.

Del Valle-Zermeño, R.; Formosa, J.; Prieto, M.; Nadal, R.; Niubó, M.; and Chimenos, J. M. (2014). "Pilot-scale road subbase made with granular material formulated with MSWI bottom ash and stabilized APC fly ash: Environmental impact assessment" *Journal of Hazardous Materials*. 266, 132-140.

Du, L.; Lukefahr, E.; and Naranjo, A. (2012). "Texas Department of Transportation Fly Ash Database and the Development of Chemical Composition-Based Fly Ash Alkali-Silica Reaction Durability Index." *ASCE Journal of Materials in Civil Engineering*, 25, 70-77.

Duxson, P., Fernández-Jiménez, A., Provis, J. L., Lukey, G. C., Palomo, A., & Van Deventer, J. S. J. (2007). "Geopolymer technology: the current state of the art." *Journal of Materials Science*, 42 (3), 2917-2933.

Duxson, P.; Provis, J. L.; Lukey, G. C.; Mallicoat, S. W.; Kriven, W. M.; and Van Deventer, J. S. (2015). "Understanding the relationship between geopolymer composition,

microstructure and mechanical properties." *Colloids and Surfaces A: Physicochemical and Engineering Aspects*, 269 (1-3), 47-58.

Elahi, A.; Basheer, P. A. M.; Nanukuttan, S. V.; and Khan, Q. U. Z. (2010). "Mechanical and durability properties of high performance concretes containing supplementary cementitious materials." *Construction and Building Materials*, 24 (3), 292-299.

Erdoğdu, K. and Türker, P. (1998). "Effects of fly ash particle size on strength of Portland cement fly ash mortars." *Cement and Concrete Research*, 28 (9), 1217-1222.

Feng, D.; Xie, N.; Gong, C.; Leng, Z.; Xiao, H.; Li, H.; Shi, X. (2013). "Portland cement paste modified by TiO2 nanoparticles: A microscopic perspective." *Industrial & Engineering Chemistry Research*, 52 (33), 11575-11582.

Fytianos, K.; Tsaniklidi, B.; and Voudrias, E. (1998). "Leachability of heavy metals in Greek fly ash from coal combustion." *Environment International*, 24, 477-486.

Gartner, E. (2004). "Industrially interesting approaches to "low-CO_2" cements." *Cement and Concrete Research*, 34 (9), 1489-1498.

Gomes, S., Fran çois, M., Abdelmoula, M., Refait, P., Pellissier, C., and Evrard, O. (1999). "Characterization of magnetite in silico-aluminous fly ash by SEM, TEM, XRD, magnetic susceptibility, and Mössbauer spectroscopy." *Cement and Concrete Research*, 29 (11), 1705-1711.

Go ñi, S.; Guerrero, A. (2007). "SEM/EDX characterization of the hydration products of Belite cements from class C coal fly ash." *Journal of the American Ceramic Society*, 90 (12), 3915-3922.

Guerrero, A., Goñi, S., Campillo, I., and Moragues, A. (2004). "Belite cement clinker from coal fly ash of high Ca content: optimization of synthesis parameters." *Environmental Science and Technology*, 38 (11), 3209-3213.

Habert, G.; d'Espinose de Lacaillerie, J. B.; and Roussel, N. (2011). "An environmental evaluation of geopolymer based concrete production: reviewing current research trends." *Journal of Cleaner Production*, 19 (11), 1229-1238.

Hasanbeigi, A.; Price, L.; and Lin, E. (2012). "Emerging energy-efficiency and CO_2 emission-reduction technologies for cement and concrete production: A technical review." *Renewable and Sustainable Energy Reviews*, 16 (8), 6220-6238.

Johari, M.; Brooks, J. J.; Kabir, S.; and Rivard, P. (2011). "Influence of supplementary cementitious materials on engineering properties of high strength concrete." *Construction and Building Materials*, 25, 2639-2648.

Johnson, C. A.; Kersten, D. M. (1999). "Solubility of Zn(II) in association with calcium silicate hydrates in alkaline solution." *Environmental Science and Technology*, 33 (13), 2296-2298.

Kayali, O. and Sharfuddin A. M. (2013). "Assessment of high volume replacement fly ash concrete-concept of performance index." *Construction and Building Materials*, 39, 71-76.

Khatri, R. P.; Sirivivatnanon, V.; and Gross, W. (1995). "Effect of different supplementary cementitious materials on mechanical properties of high performance concrete." *Cement and Concrete Research*, 25 (1), 209-220.

Kutchko, B. G.; Kim, A.G. (2006). "Fly ash characterization by SEM-EDS." *Fuel*, 85 (17-18), 2537-2544.

Lei, Y.; Zhang, Q.; Nielsen, C.; and He, K. (2011). "An inventory of primary air pollutants and CO$_2$ emissions from cement production in China, 1990-2020." *Atmospheric Environment*. 45 (1), 147-154.

Lemougna, P.N., MacKenzie, K.J., Jameson, G.N., Rahier, H., and Melo, U.C. (2013). "The role of iron in the formation of inorganic polymers (geopolymers) from volcanic ash: a 57Fe Mössbauer spectroscopy study." *Journal of Materials Science*, 48(15), 5280-5286.

Lothenbach, B.; Scrivener, K.; and Hooton, R. D. (2011). "Supplementary cementitious materials." *Cement and Concrete Research*, 41 (12), 1244-1256.

Ma, B.; Qi, M.; Peng, J.; and Li, Z. (1999). "The compositions, surface texture, absorption, and binding properties of fly ash in China." *Environment international*, 25 (4), 423-432.

Malvar, L. J.; Lenke, L. R. (2006). "Efficiency of fly ash in mitigating alkali-silica reaction based on chemical composition." *ACI Materials Journal*, 103 (5), 319-326.

McLellan, B. C.; Williams, R. P.; Lay, J.; Van Riessen, A.; and Corder, G. D. (2011). "Costs and carbon emissions for geopolymer pastes in comparison to ordinary portland cement." *Journal of Cleaner Production*, 19 (9-10), 1080-1090.

Oh, J. E.; Moon, J.; Oh, S. G. et al. (2012). "Microstructural and compositional change of NaOH-activated high calcium fly ash by incorporating Na-aluminate and co-existence of geopolymeric gel and C–S–H (I)." *Cement and Concrete Research*, 42 (5), 673-685.

Pace, M. L.; Telesca, A.; Marroccoli, M. et al. (2011). "Use of industrial byproducts as alumina sources for the synthesis of calcium sulfoaluminate cements." *Environmental Science and Technology*, 45, 6124-6128.

Palomo, A.; Grutzeck, M. W.; and Blanco, M. T. (1999). "Alkali-activated fly ashes: a cement for the future." *Cement and Concrete Research*, 29, 1323-1329.

Paya, J.; Monzo, J.; Borrachero, M. V. et al. (1998). "Thermogravimetric methods for determining carbon content in fly ashes." *Cement and Concrete Research*, 28 (5), 675-686.

Pelisser, F.; Steiner, L. R.; Bernardin, A. M. (2012). "Recycling of porcelain tile polishing residue in Portland cement: hydration efficiency." *Environmental Science and Technology*, 46 (4), 2368-2374.

Popovic, A.; Djordjevic, D.; and Polic, P. (2001). "Trace and major element pollution originating from coal ash suspension and transport processes." *Environment International*, 26 (4), 251-255.

Rajabipour, F., Weiss J., (2007). "Electrical conductivity of drying cement paste." *Materials and Structures*. 40 (10), 1143–1160.

Ramezanianpour, A. A. (2014). "Fly Ash." *Cement Replacement Materials*. Springer, Heidelberg-New York-Dordrecht-London, 47-156.

Reddy, D. V.; Edouard, J. B.; and Sobhan, K. (2012). "Durability of Fly ash-based geopolymer structural concrete in the marine environment." *Journal of Materials in Civil Engineering*, 25(6), 781-787.

Reijnders, L. (2007). "Cleaner phosphogypsum, coal combustion ashes and waste incineration ashes for application in building materials: A review." *Building and Environment*, 42 (2), 1036-1042.

Richardson, I.G. (1999). "The Nature of C-S-H in Hardened Cements." *Cement and Concrete Research*. 29 (8), 1131-1147.

Roskos C.; Cross D.; Berry M.; and Stephens J. (2011). "Identification and verification of self-cementing fly ash binders for "green" concrete." *Proceedings of the 2011 world of coal*

ash (WOCA) conference. The American Coal Ash Association. May 9-12, Denver, CO, USA.

Rostami, H.; Brendley W. (2003). "Alkali ash material: a novel fly ash-based cement." *Environmental Science and Technology*, 37 (15), 3454-3457.

Roy, A.; Schilling, P.; Eaton, H. (1995). "Alkali activated class C fly ash cement." U.S. Patent 5,435,843, July 25.

Sarıdemir, M. (2014). "Effect of specimen size and shape on compressive strength of concrete containing fly ash: Application of genetic programming for design." *Materials & Design*, 56, 297-304.

Schneider M.; Romer M.; Tschudin M.; Bolio H. (2011). "Sustainable cement production - present and future." *Cement and Concrete Research*. 41 (7), 642-50.

Shi, C. (1996). "Strength, pore structure and permeability of alkali activated slag mortars." *Cement and Concrete Research*, 26 (12), 1789-1799.

Shi, C.; Roy, D.; and Krivenko, P. (2005). "Alkali-activated cements and concretes." *Taylor & Francis*. London and New York.

Shi, X.; Xie, N.; Fortune, K.; and Gong J.. (2012). "Durability of steel reinforced concrete in chloride environments: An overview." *Construction and Building Materials*, 30, 125-138.

Shi, X.; Yang, Z.; Liu, Y.; and Cross, D. (2011). "Strength and corrosion properties of portland cement mortar and concrete with mineral admixtures." *Construction and Building Materials*, 25(8), 3245-3256.

Singhal, A., Tewari, V. K., & Prakash, S. (2008). "Utilization of treated spent liquor sludge with fly ash in cement and concrete." *Building and Environment*, 43 (6), 991-998.

Standard, A. S. T. M. (2011). C1157. Standard Performance Specification for Hydraulic Cement.

Standard A. S. T. M. (2012). C618. Specification for Coal Fly Ash and Raw or Calcined Natural Pozzolan for Use in Concrete.

Standard A. S. T. M. (2007). C150-07. Standard Specification for Portland Cement.

Standard A. S. T. M. (2007). C1437. Standard Test Method for Flow of Hydraulic Cement Mortar

Standard A. S. T. M. (2013). C109. Standard Test Method for Compressive Strength of Hydraulic Cement Mortars

Taylor, H.F.W. (1986). Proposed Structure for Calcium Silicate Hydrate Gel. *Journal of the American Ceramic Society*. 69 (6), 464-467.

Taylor, Harry F.W. (1997). "Cement chemistry." *Thomas Telford*. London.

Thomas, J.J.; Jennings, H.M.; and Allen, A.J. (1998). "Determination of the Neutron Scattering Contrast of Hydrated Portland Cement Paste Using H2O/D2O Exchange." *Advanced Cement Based Materials*. 7 (3-4), 119-122.

Van Dam, T. J.; Smartz, B. W. (2010). "Use of Performance-Specified (ASTM C1157) Cements in Colorado Transportation Projects: Case Studies." *Transportation Research Board 89th Annual Meeting. Washington, D.C.* 10-1355.

Veranth, J. M.; Smith, K. R.; Huggins, F. et al. (2000). "Mössbauer spectroscopy indicates that iron in an aluminosilicate glass phase is the source of the bioavailable iron from coal fly ash." *Chemical Research in Toxicology*, 13 (3), 161-164.

Ward, C. R.; French, D. (2006). "Determination of glass content and estimation of glass composition in fly ash using quantitative X-ray diffractometry." *Fuel*, 85 (16), 2268-2277.

Xie, N.; Bell J.; and Kriven W. M. (2010). "Fabrication of structural leucite glass-ceramics from

    potassium-based geopolymer precursors." *Journal of the American Ceramic Society*. 93

    (9), 2644-2649.

Yang, Z.; Hollar, J.; He, X.; Shi, X. (2011). "A self-healing cementitious composite using oil

    core/silica gel shell microcapsules." *Cement and Concrete Composites*, 33 (4), 506-512.

Yang, Z.; Shi, X.; Creighton, A. T.; Peterson, M. M. (2009). "Effect of styrene-butadiene rubber

    latex on the chloride permeability and microstructure of portland cement mortars."

    Construction and Building Materials, 23(6), 2283-2290.

Yost, J. R.; Radlińska, A.; Ernst, S. et al. (2013a). "Structural behavior of alkali activated fly ash

    concrete. Part 1: mixture design, material properties and sample fabrication." *Materials*

    and Structures, 46, 435-447.

Yost, J. R.; Radlińska, A.; Ernst, S. et al. (2013b). "Structural behavior of alkali activated fly ash

    concrete. Part 2: structural testing and experimental findings." *Materials and Structures*,

    46, 449-462.

Yüksel, İ., Bilir, T., & Özkan, Ö. (2007). "Durability of concrete incorporating non-ground blast

    furnace slag and bottom ash as fine aggregate." *Building and Environment*, 42 (7), 2651-

    2659.

Zhang, T.; Gao, P.; Gao, P.; Wei, J.; and Yu, Q. (2013). "Effectiveness of novel and traditional

    methods to incorporate industrial wastes in cementitious materials-An overview."

    Resources, Conservation and Recycling, 74, 134-143.